Numerical Simulation of Regulating Performance of Direct-Operated Pressure Regulator for a Microirrigation Lateral

Chen Zhang and Guangyong Li

College of Water Resources and Civil Engineering,
China Agricultural University, Beijing 100083, China
swzhangchen@163.com, lgyl@cau.edu.cn

Abstract. A lateral inlet direct-operated pressure regulator is a novel device for microirrigation system that ensures the equal operating pressure of the lateral inlet required for high uniformity. This study develops a computational fluid dynamics (CFD) model in combination with inlet pressure and regulation assembly displacement to analyze the outlet pressure of the pressure regulator. The model is validated by a comparison of experimental measurements, and the predicted results show good agreement. The effects of the regulation assembly displacement and geometrical structure (regulation assembly inlet height) on regulating performance are investigated. Results show that the magnitude of the regulation assembly movement affecting by inlet pressure, preset pressure, and flow rate significantly changes in the beginning of the regulation range and then changes slowly. The spring parameters can be designed according to the force–displacement characteristic (the F–L_v curve) of the T-shape regulating plunger. A greater regulation assembly inlet height corresponds to a lower preset pressure and less sensitivity of pressure loss to the movement of the regulation assembly. The pressure distribution through the regulator provides an improved understanding of the pressure difference in the regulating plunger with various displacements. The CFD model can reflect the motion characteristics of the regulation assembly and reveal the key factor of the regulator design. The results form the sound basis for future design and performance optimization of pressure regulator.

Keywords: microirrigation, pressure regulator, pressure regulating performance, CFD analysis.

1 Introduction

A microirrigation system located in a hilly and mountainous area or in a large submain unit will have varying lateral inlet pressure considerably along the submain because of terrain slope and hydraulic friction loss. Pressure regulators perform a critical function in ensuring the lateral inlet pressure required for high uniformity.

Bernuth and Baird [1] tested three brands of agricultural irrigation pressure regulators to characterize their performance. A line segments separate and linear

D. Li and Y. Chen (Eds.): CCTA 2014, IFIP AICT 452, pp. 285–303, 2015.
DOI: 10.1007/978-3-319-19620-6_34

regression computer program was developed to determine the preset pressure and regulation range. Their work serves as a reference for testing and performance evaluation. According to Tian et al. [2], the main factors affecting pressure regulator performance are spring stiffness coefficient, spring length, upriver and downriver areas of the regulating part, and space between the regulating part and block cap. An orthogonal experiment was conducted to quantificationally analyze the effects of those factors on preset pressure. The results show that a linear relationship exists between the four factors and the preset pressure.

The development of computational fluid dynamics (CFD) has increased the accuracy of predicting the fluid characteristics and flow field distribution inside a fluid machinery. Many researches have been made on the flow prediction of relief valves and safety valves. Mokhtarzadeh-Dehghan et al. [3] conducted a finite element study on the flow of oil through a hydraulic pressure relief valve of the differential angle type. The results show that the total force on the plunger increases approximately linearly with increasing plunger lift. Depster et al. [4] and Depster and Elmayyah [5] reported a 2D representation by using Reynolds-averaged Navier–Stokes equations and standard k–ε turbulence model to investigate the force-lift and flow-lift characteristics of a spring-operated safety relief valve. Han et al. [6] presented the steady and transient characteristics of a Contra-push check valve (CPCV) simulated by CFD codes. Results show that the size of the gap between plug and sleeve is a key factor in CPCV design, another one is annular area of the plug. Chattopadhyay et al. [7] presented the simulating investigations of the flow through a spool type pressure regulating valve at different opening and different pressure drop. Song et al. [8] developed a simplified dynamic model to simulate the dynamic characteristics of a conventional pressure relief valve. The lift force coefficient of the valve at several fixed lifts was calculated using the static CFD analysis and was then imported into the dynamic model as the inherent characteristic of the valve to predict the plug lift during the reclosing process. Shahani et al. [9] performed dynamic simulation models to analyze the regulator performance of a high pressure regulator. The regulator behavior consist of the output pressure change versus time, the displacement of the moving parts versus time, and the regulator mass flow rate versus time were obtained. Beune et al. [10] developed a multi-mesh numerical valve model to analyze the opening characteristic of high-pressure safety valves. Song et al. [11] developed a numerical model including moving mesh techniques to investigate the fluid and dynamic characteristics of a direct-operated safety relieve valve. The effects of design parameters on flow forces acting on the disc and the lift of the valve are analyzed and compared.

For a lateral inlet direct-operated pressure regulator, the regulation assembly moves under different inlet pressure and flow rate conditions. However, the previous experimental studies pay no attention to the motion characteristic of the regulation assembly and its influence to the regulating performance. In this paper, a mathematical model combined with regulation assembly displacement and geometrical structure is developed to simulate the hydraulic performance of pressure regulator by CFD approaches. Basing on steady CFD analysis of the pressure regulator at several fixed displacements, the relationship among regulator inlet pressure, regulation assembly displacement, and the outlet pressure are obtained. The results of this study can be used as reference for the design and the performance optimization of the pressure regulator.

2 Working Principle of a Pressure Regulator

A lateral inlet direct operated pressure regulator mainly consists of eight parts (Fig. 1). The regulation assembly plays a part in regulating the outlet pressure, which consists of the regulation assembly inlet, spring, and T-shape regulating plunger. When water flows across the pressure regulator, head loss occurs in the gap between the regulation assembly inlet and the top surface of the T-shape regulating plunger. Thereafter, the hollow plunger transmits the water to the outlet.

When the inlet pressure is below the preset pressure, the outlet pressure increases with the inlet pressure increasing. The T-shape regulating plunger stay stationary for the pressure difference induced force on the plunger is less than the pre-stressed spring force (Fig. 2a). As the inlet pressure is higher than the preset pressure, the force acting on the plunger that overcomes the preloading of the spring forces the plunger to move against the flow direction (Fig. 2b). Therefore, the gap becomes narrow, and the friction loss increases. Consequently, the outlet pressure decreases and ensures the regulator to maintain its constant outlet pressure. When the inlet pressure decreases from a high value to the preset pressure, the movement process of the regulation assembly becomes the opposite.

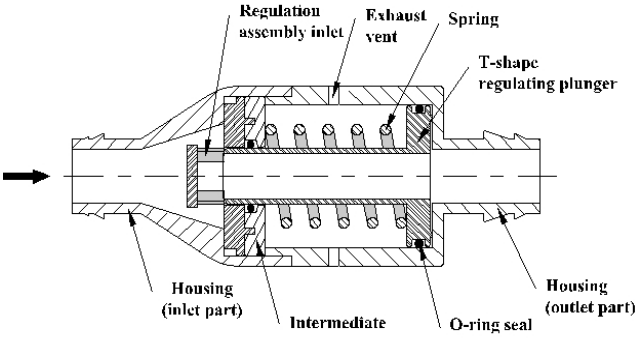

Fig. 1. Schematic cross-section of a pressure regulator

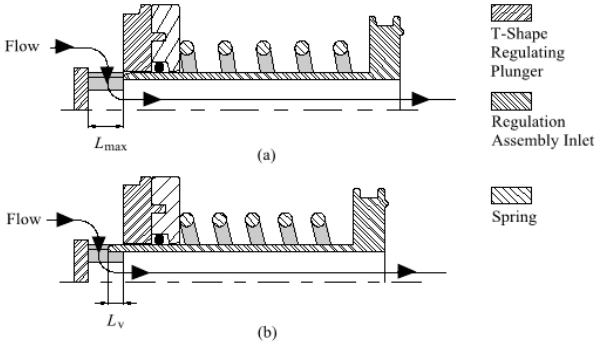

Fig. 2. Regulating process of a pressure regulation assembly (the axisymmetric part) (a) Before regulation range and (b) regulation range

3 Numerical Methods

3.1 Mathematical Models

Outlet Pressure and Displacement Expression

On the basis of the flow rate formula, the flow rate of the pressure regulator is expressed as follows:

$$Q = C\sqrt{\frac{\Delta P}{\rho}} \quad , \tag{1}$$

where Q is the flow rate throughout the pressure regulator, L/h, and is calculated as $Q=vA$, where v is the average velocity in the pipe, m/s and A is the nominal cross-section, mm^2; ΔP is the pressure difference between the pressure regulator inlet and the outlet, Pa; C is the flow coefficient; and ρ is the water density, 1000 kg/m^3.

The flow area of the regulation assembly inlet changes with different pressure drops (Fig. 2).The following shows the flow rate throughout the pressure regulator when the regulation assembly is at any displacement Q_v and the flow rate of the pressure regulator when the regulation assembly is at initial position Q_{max}:

$$Q_v = C_v\sqrt{\frac{\Delta P}{\rho}} \ , \quad Q_{\max} = C_{\max}\sqrt{\frac{\Delta P}{\rho}} \quad .$$

When the pressure differences between the pressure regulator inlet and the outlet are the same, the following equation is obtained:

$$\frac{Q_v}{Q_{\max}} = \frac{C_v}{C_{\max}} \quad . \tag{2}$$

When the change in the flow area is caused by the displacement of the regulation assembly, the expression for Q_v/Q_{max} becomes the following:

$$\frac{Q_v}{Q_{\max}} = f\left(\frac{L_{\max} - L_v}{L_{\max}}\right) \quad , \tag{3}$$

where L_v is the axial displacement of the T-shape regulating plunger, i.e., the distance the plunger moves from the initial position to the upstream, mm; L_{max} is the maximal axial displacement of the plunger, i.e., the height of the regulation assembly inlet, mm.

From Equation (1), the pressure difference between the pressure regulator inlet and outlet ΔP is expressed as follows:

$$\Delta P = \frac{\rho Q^2}{C^2} \quad . \tag{4}$$

By combining Equations (2) to (4), Equation (4) can be written as

$$\Delta P = \frac{\rho Q^2}{f(\frac{L_{\max} - L_v}{L_{\max}})^2 C_{\max}{}^2} \quad . \tag{5}$$

The outlet pressure equation of the pressure regulator can be written as

$$P_{out} = P_{in} - \Delta P = P_{in} - \frac{\rho Q^2}{f(1-\frac{L_v}{L_{\max}})^2 C_{\max}{}^2} \quad , \tag{6}$$

where P_{in}, P_{out} are the inlet and outlet pressures of the pressure regulator, respectively, Pa. The function expressions are provided by the results from the numerical simulation in the following section.

Equations of the Mechanical Models

Fig. 3 shows the force analysis of the T-shape regulating plunger. Friction force is assumed to be negligible. A force balance equation of the plunger is formulated as

$$F_{\text{s}} + P_1 A_1 = P_2 A_2 \quad , \tag{7}$$

where the spring force F_{s} is given by

$$F_{\text{s}} = K_s \left(L_0 + L_v \right) \quad . \tag{8}$$

The force acting on the T-shape regulating plunger F is induced by the pressure difference between the top and bottom surfaces of the plunger. The expression for force F then becomes

$$F = P_2 A_2 - P_1 A_1 \quad , \tag{9}$$

where K_{s} is the spring stiffness, N/mm; L_0 is the pre-stressed spring length, mm; P_1, P_2 are the pressures on the top and bottom surfaces of the T-shape regulating plunger, respectively, Pa; A_1, A_2 are the areas of the top and bottom surfaces of the plunger, respectively. The values of A_1, A_2 are 12.7and 510mm^2, respectively.

Governing Equations and Turbulence Models

To describe the 3D flow phenomenon in a pressure regulator, uncompressible Navier–Stokes equations are numerically solved in the commercial software package ANSYS FLUENT.

Conservation of mass is expressed as

$$\frac{\partial}{\partial x_i} u_i = 0 \quad . \tag{10}$$

Conservation of momentum is expressed as

$$\frac{\partial}{\partial t}(\rho u_i) + \frac{\partial}{\partial x_i}(\rho u_i u_j) = -\frac{\partial p}{\partial x_i} + \frac{\partial \tau_{ij}}{\partial x_j} + \rho g_i + F_i \quad , \tag{11}$$

where u_i is the fluid velocity component in the i direction, g_i is the acceleration of the gravity component in the i direction, $\tau_{ij} = \left[\mu_{eff} (\frac{\partial u_i}{\partial x_j} + \frac{\partial u_j}{\partial x_i}) \right] - \frac{2}{3} \mu_{eff} \frac{\partial u_l}{\partial x_l} \delta_{ij}$, and δ_{ij} is the Kronecker symbol.

The turbulent kinetic energy, k, and its rate of dissipation, ε, are obtained from the following transport equations in the standard k–ε model:

$$\frac{\partial}{\partial t}(\rho k) + \frac{\partial}{\partial x_i}(\rho k u_i) = \frac{\partial}{\partial x_j}\left[\left(\mu + \frac{\mu_t}{\sigma_k} \right) \frac{\partial k}{\partial x_j}) \right] + G_\kappa - \rho \varepsilon \quad , \tag{12}$$

and

$$\frac{\partial}{\partial t}(\rho \varepsilon) + \frac{\partial}{\partial x_i}(\rho \varepsilon u_i) = \frac{\partial}{\partial x_j}\left[\left(\mu + \frac{\mu_t}{\sigma_\varepsilon} \right) \frac{\partial \varepsilon}{\partial x_j} \right] + C_{1\varepsilon} \frac{\varepsilon}{k} G_k - C_{2\varepsilon} \rho \frac{\varepsilon^2}{k} \quad , \tag{13}$$

where μ is the coefficient of dynamic viscosity; G_κ is the generation of turbulence kinetic energy due to the mean velocity gradients; and the model constants C_μ, $C_{1\varepsilon}$, $C_{2\varepsilon}$, σ_k, and σ_ε have the following value: C_μ=0.09, $C_{1\varepsilon}$=1.44, $C_{2\varepsilon}$=1.92, σ_k=1.0, and σ_ε=1.22.

Equation (6) shows that the outlet pressure P_{out} is calculated by L_v, and Q_v. Equations (7) – (9) indicate that the spring stiffness K_s and pre-stressed spring length L_0 are determined by L_v, and F. However, the value of L_v in a certain inlet pressure cannot be obtained directly from the experiment. Hence, a series of discrete models at different displacements are established, and then the F–L_v curve is fitted with the CFD results at different positions. The procedure for the F–L_v curve calculation of the pressure regulator is shown in Fig. 4.

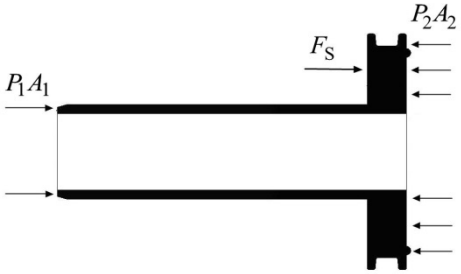

Fig. 3. Force acting on the T-shape regulating plunger

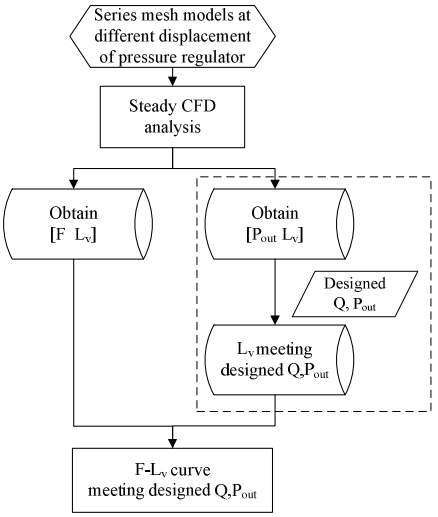

Fig. 4. Strategy for obtaining the F–L_v curve

3.2 Computational Mesh

To reduce computational time, the computational domain is reduced to half of the full 3D pressure regulator model. Considering the fully developed fluid, the pipeline was extended to 5 times the nominal diameter in the inlet and outlet. The full 3D structured hexahedral mesh is generated by using the commercial mesh generator ICEM CFD (Fig. 5). To obtain good quality and to represent the details of the regulation assembly inlet, a domain decomposition method that splits the entire complex pressure regulator interior domain into several subdomains is applied [12]. The interface boundary is set to the corresponding zones of the subdomains. Mesh quality has been rigorously checked for parameters, such as skewers and aspect ratio. The mesh quality metrics in ICEM CFD shows that the mesh quality of the model is greater than 0.65, which is sufficient for this case. Mesh independence for a 3D simulation is undertaken by using 4 different mesh levels composed of approximately 100,000, 200,000, 500,000, and 800,000 nodes, respectively. The mesh with 500,000 nodes is selected for the numerical analysis. The number of mesh models range from 490,000 to 540,000 for the different displacement models.

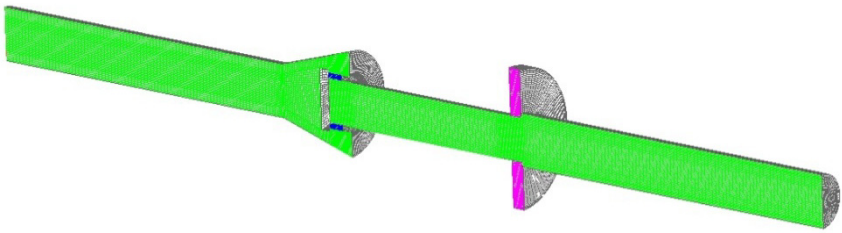

(a) Entire computational domain(L_v = 2 mm)

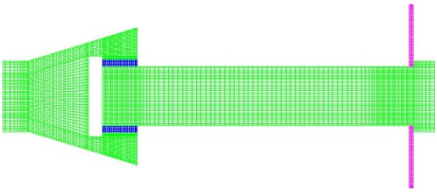

(b) Partial view of mesh on the symmetry plane (L_v = 0 mm)

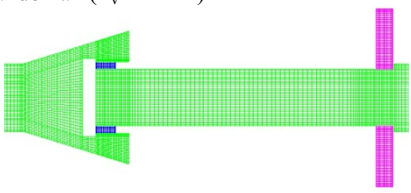

(c) Partial view of mesh on the symmetry plane (L_v = 2 mm)

Fig. 5. Computational mesh of the pressure regulator

3.3 Boundary Conditions and Solution Strategy

Different pressure values are specified on the inlet and outlet. No-slip boundary condition has been assumed on all walls. On the symmetry plane, the scalar variables and the scalar variable gradients normal to the boundary were set to zero. The reference pressure over the whole domain was defined as 101,325 Pa. Several values of inlet pressure were specified in the range from 0.075MPa to 0.55MPa, which were contained in the range of the experimental inlet pressure.

The second-order upwind scheme was used for descretization of momentum and the SIMPLE algorithm was applied for coupling of the pressure and velocity, the standard k-ε model for turbulent flow. The continuity equation and momentum were considered converged when the residuals for each of variables reached to the order 10^{-5}.

4 Results and Discussion

4.1 Outlet Pressure and Displacement Expression

Fig. 6 shows the predicted flow rate relative to the maximum flow rate in each fixed displacement for the pressure regulators of different regulation assembly inlet heights. The regression equation is obtained as follows:

$$\frac{Q_v}{Q_{\max}} = a\ln(1-\frac{L_v}{L_{\max}})+b \quad . \tag{14}$$

The values of coefficients for different regulation assembly inlet heights are given in Table 1. The maximum flow coefficient is obtained by Equation (1). By substituting Equations (14) into Equation (6), the following form can be obtained:

$$P_{out} = P_{in} - \frac{\rho Q^2}{[a\ln(1-\frac{L_v}{L_{\max}})+b]^2 C_{\max}{}^2} \quad . \tag{15}$$

Table 1. a, b, and $C_{\max}$ values of the pressure regulator for different $L_{\max}$.

$L_{\max}$/mm	4	5	6	7
a	0.3474	0.3442	0.309	0.2939
b	1.0368	1.0567	1.0756	1.0994
$C_{\max}$	4.80E-05	4.93E-05	5.00E-05	5.01E-05

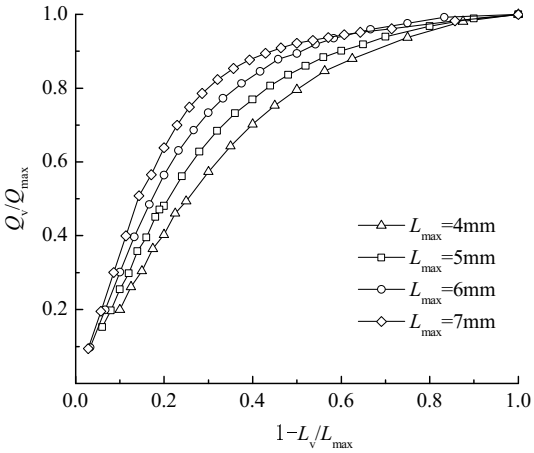

Fig. 6. Relative flow rate $Q_v/Q_{\max}$ change with the relative displacement $L_v/L_{\max}$

Fig. 7 shows the outlet pressure change in different displacements under different inlet pressures as calculated by Equation (15). The outlet pressure slowly changes when the displacement is small. When the displacement increases, the outlet pressure rapidly decreases. A higher inlet pressure corresponds to a greater variation of outlet pressure when the displacement is large. The flow rate affects the outlet pressure.

Under the same inlet pressure, the comparison between Figs. 7(a) and (b) shows that a higher the flow rate corresponds to a lower outlet pressure. An ideal regulator can maintain a constant outlet pressure regardless of the inlet pressure or flow rate, provided that the inlet pressure is above the preset pressure. The constant preset pressure 0.05 and 0.1MPa, which represent the two straight lines, are plotted in Fig. 7. The intersection of the straight lines and outlet pressure curves provide the value of displacement that the T-shape regulating plunger will reach under that inlet pressure (Fig. 8).

The data shows the law of movement of the regulation assembly. The displacement of the T-shape regulating plunger increases rapidly as the inlet pressure increases at the beginning of the regulating process. When the inlet pressure is greater than 0.2MPa (Fig.8 a), the distance increases slightly from 4 mm to 4.5 mm. Comparing the two motions with the same flow rate but different preset pressure show that the regulation assembly set low preset pressure moves first. However, the displacements are almost the same when the inlet pressure is high. A decrease in flow rate tends to advance the motion of the regulation assembly and increases displacement (Fig. 8).

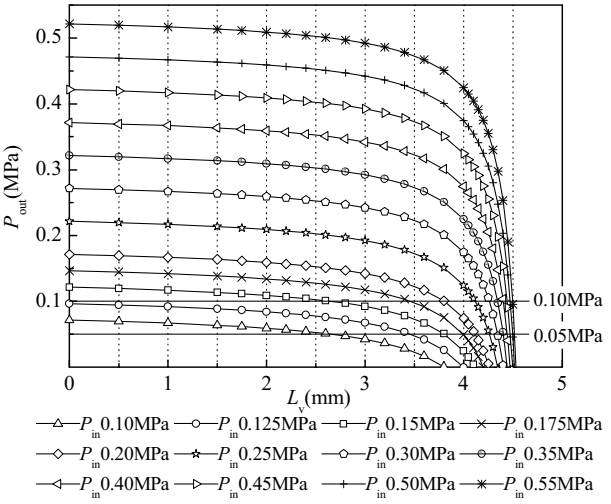

(a)Q = 1000 L/h

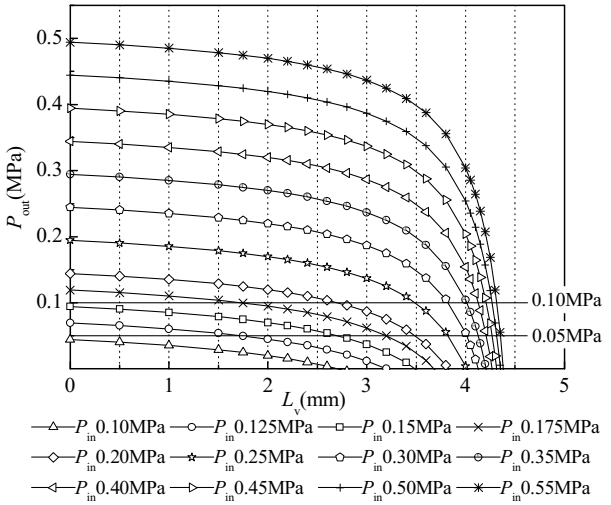

(b)Q = 1400 L/h

Fig. 7. Outlet pressure change with different displacements at different inlet pressures (L_{max} = 5 mm)

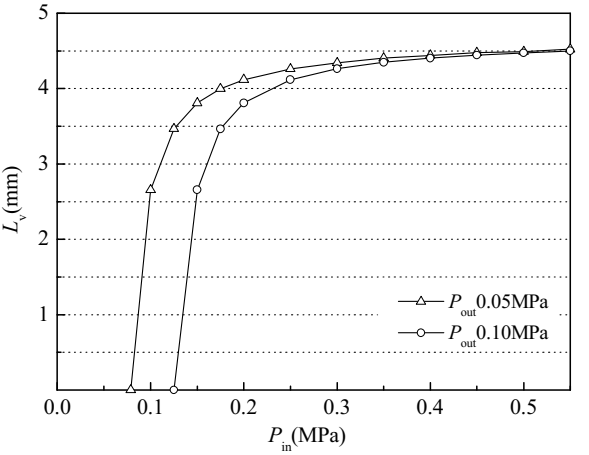

(a)Q = 1000 L/h

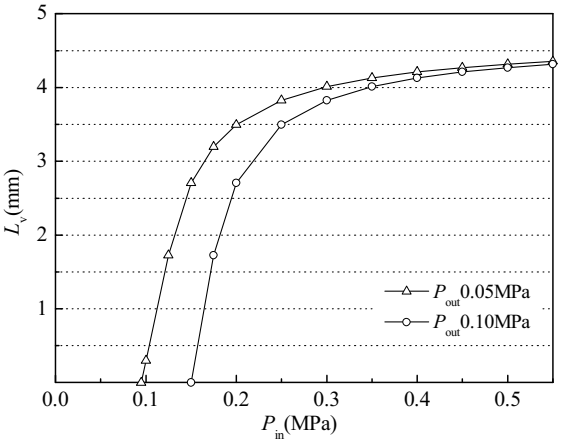

(b)Q = 1400 L/h

Fig. 8. Displacement of the T-shape regulating plunger at different inlet pressures(L_{max} = 5 mm)

4.2 Displacement-Force Characteristics

Fig. 9 shows the axial force induced by the pressure difference on the T-shape regulating plunger for two preset pressure conditions. When the pressure difference between the inlet and outlet is the same, the force acting on the plunger increases with increasing displacement. A quadratic polynomial functional relationship is analyzed between the displacement and the force. A high preset pressure leads to a large force magnitude. Therefore, a large spring per-stressed force should be exerted for the pressure regulator with a high preset pressure.

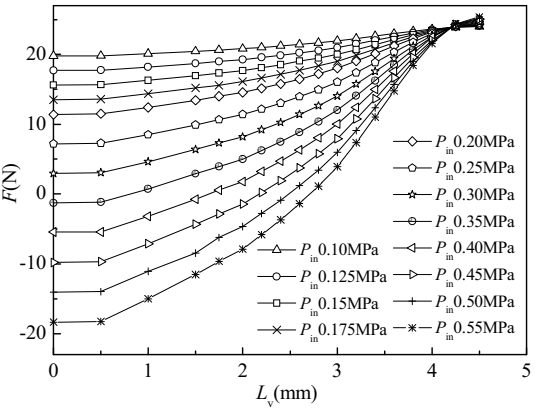

(a) P_{out} = 0.05 MPa

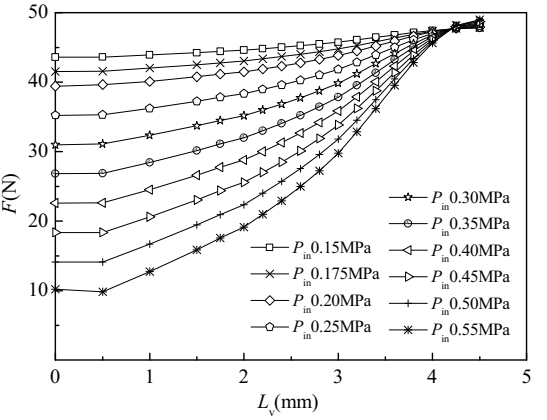

(b) P_{out} = 0.1 MPa

Fig. 9. Predicted force on the T-shape regulating plunger at different inlet pressures (L_{max} = 5 mm)

By mapping Figs. 8 to 9, the relationship between the force acting on the T-shape regulating plunger (F) and the displacement (L_v) meeting the preset pressure and flow rate requirements was obtained Fig. 10 shows the F–L_v curves for the different flow rates with preset pressures of 0.05 and 0.1MPa. The pressure induced force has a nonlinear relationship with the displacement. When the displacement is smaller than 3 mm, the force acting on the plunger slightly changes. The force increases sharply when the plunger increases up to the maximum displacement. Note that, as the spring force satisfies the Hooke's Law, the spring force (the F_s–L_v line) will intersect with the F–L_v curve but cannot coincide with the curve. Therefore, the reasonable spring parameters, i.e., spring stiffness and pre-stressed spring length, can be designed by providing the minimum deviation between the F_s–L_v line and the F–L_v curve.

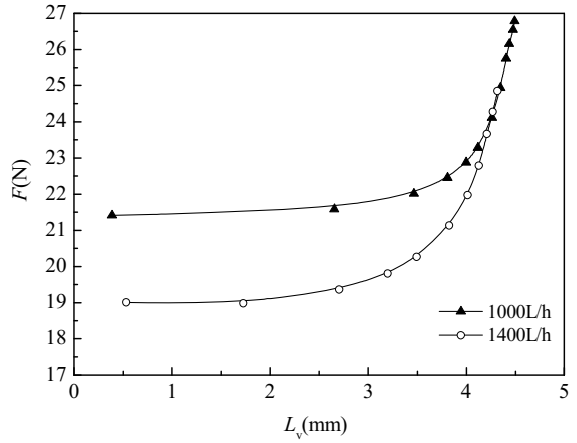

(a) P_{out} = 0.05 MPa

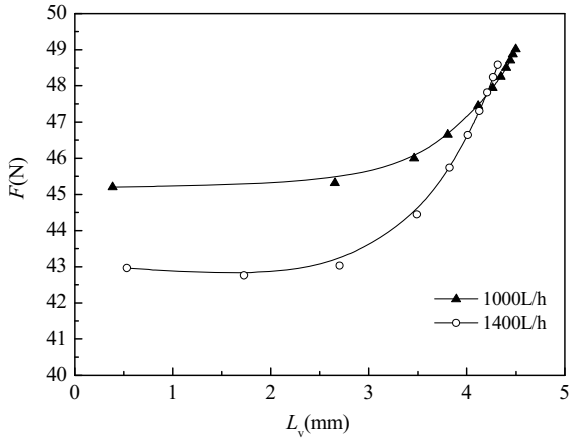

(b) P_{out} = 0.1 MPa

Fig. 10. Fitted F– L_v curves (L_{max} = 5 mm)

The flow rate of the pressure regulator is not a constant value but a range of values, which means that the outlet pressure variation caused by the flow rate variation does not exceed the limit within the flow rate range. In this paper, a certain flow rate that meets the requirement is considered as the upper limit of the discharge.

4.3 Effect of the Regulation Assembly Inlet Height

The hydraulic behavior of the pressure regulator is characterized by the local pressure drop introduced by the regulator itself [13]. This pressure drop is made nondimensional by the mean dynamic pressure in the regulator. The pressure drop coefficient is expressed as follows:

$$K=\frac{2\Delta P}{\rho v^2}. \tag{16}$$

Fig. 11 shows the maximum pressure drop coefficient of the pressure regulator calculated by the mesh models in the initial position of different regulation assembly inlet heights. The maximum pressure drop coefficient (K_{max}) decreases sharply when the regulation assembly inlet height (L_{max}) changes from 4 mm to 9 mm K_{max} decreases gradually when L_{max} is greater than 9 mm. Increasing the regulation assembly inlet height can decrease the head loss of the flow through the pressure regulator, thus reducing the operating pressure(Fig. 11). However, the effect of decreasing the friction loss becomes insignificant with increasing L_{max}, and the value of L_{max} affects the volume of the pressure regulator. Therefore, a balance in the design should be considered.

The pressure drop coefficient with the changing relative displacement is shown in Fig. 12. This figure reveals the change of pressure loss inside the pressure regulator with the movement of the regulation assembly. Fig. 12 shows that a sudden increase in the pressure drop coefficient will occur when the plunger is close to the maximum

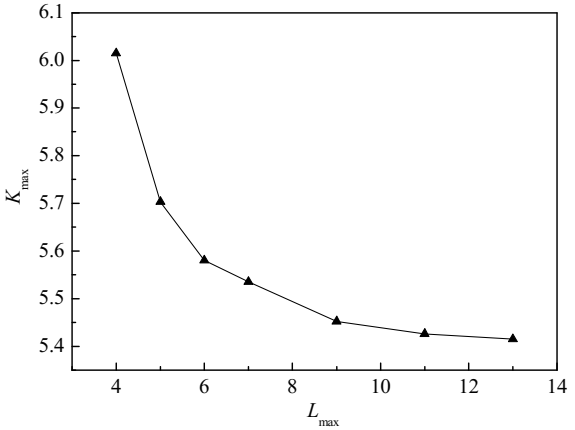

Fig. 11. Pressure drop coefficient of the pressure regulator for different regulation assembly inlet heights

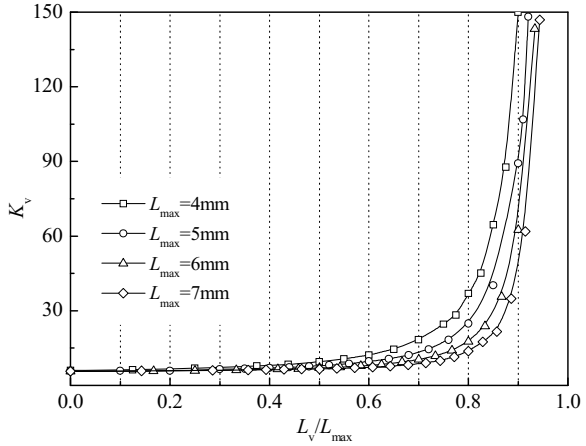

Fig. 12. Pressure drop coefficient changes with the relative displacement for different regulation assembly inlet heights

displacement. Furthermore, curve L_{max}=4 mm shows that when the displacement is over 60% of the regulation assembly inlet height, the pressure drop coefficient will begin to increase rapidly. However, the curve for L_{max}=7 mm shows a sudden increase point of approximately 80% of the regulation assembly inlet height. Therefore, increasing the regulation assembly inlet height can decrease the sensitivity of pressure loss to the movement of the regulation assembly and ensure a stable outlet pressure.

4.4 Pressure Distribution

The pressure distribution in the same inlet and outlet pressure conditions at six different displacements are shown in Fig. 13. The pressure contours are distributed densely in the regulation assembly inlet and upstream of the plunger, thus indicating that the pressure loss mainly occurs at those regions. As the T-shape regulating plunger changing its position towards the regulator inlet, the high pressure stagnates in the outer region of the regulation assembly inlet. The largest pressure drop position becomes centralized to the region between the top surface of the plunger and the regulation assembly inlet. The movement of the regulation assembly results in changes in the pressure distribution of the pressure regulator, thus, the force produced by the pressure difference between the top and bottom surfaces of the plunger is affected significantly.

(a) Full computational domain (L_v=0 mm)

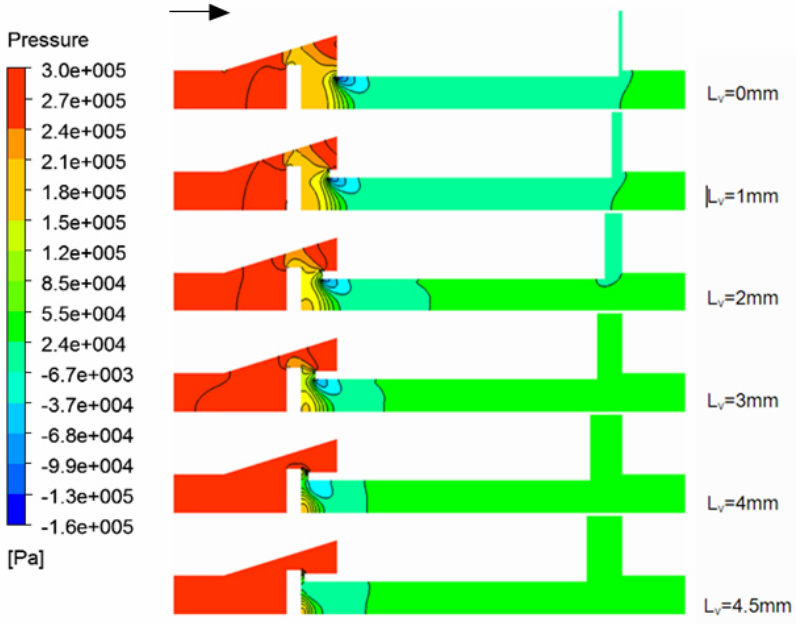

(b) Upstream and downstream regions of the T-shaped regulating plunger

Fig. 13. Pressure distribution on the symmetry plane (L_{max} = 5 mm, P_{in} = 0.3 MPa, P_{out} = 0.05 MPa)

4.5 Validation of the Computational Model

To validate the predicted results, several experiments were applied to the pressure regulator (5mm regulation assembly inlet height, 0.05MPa preset pressure, 2.31 N/mm spring stiffness, and 5.5mm pre-stressed spring length). A layout and schematic drawing of the experimental setup is shown in Fig. 14. The setup is created to measure the outlet pressure and the flow rate through the regulator in a series of inlet pressures. By substituting the tested pressure and flow rate data into Equation (15), the displacement of the T-shaped regulating plunger can be obtained (Fig. 15).

The accuracy of the numerical model was verified by modeling the geometry with the calculated displacement and repeating the CFD calculations. Fig. 16 shows a comparison of flow rates between the CFD model and experimental results. Table 2 shows the deviation of the numerical and experimental flow rates. A low flow rate is predicted before the regulation range (inlet pressure of less than 0.05MPa) (Fig. 16). This error can be accounted for by the difference in the geometrical model and testing production. Within the regulation range, the difference between the predicted and experimental flow rate is caused by the additional deviation of the calculated displacement from the real movement distance. However, the deviation between the numerical and experimental values is less than 7.3% (see Table 2), thus indicating that the numerical analysis properly predicts the actual flow in the pressure regulator and the displacement of the regulation assembly.

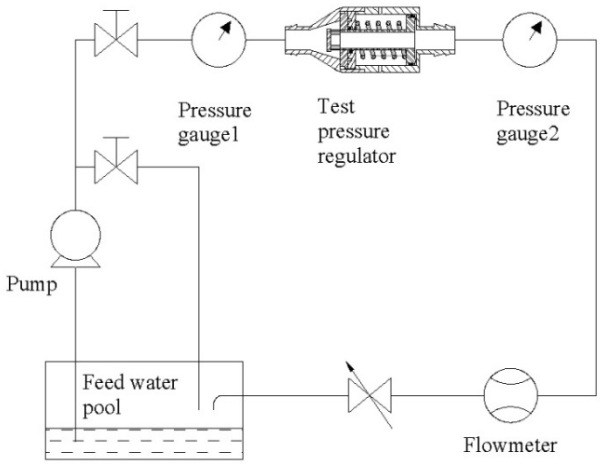

Fig. 14. Description of the testing system for the pressure regulator

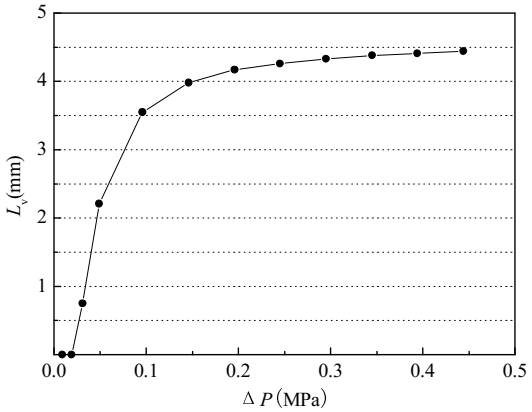

Fig. 15. Calculated displacement of the testing pressure regulator (L_{max} = 5 mm)

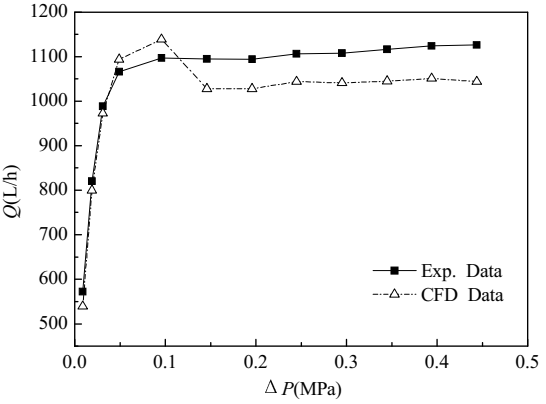

Fig. 16. Comparison of the numerical and experimental flow rates (L_{max} = 5 mm)

Table 2. Deviation of the numerical and experimental flow rates

ΔP (MPa)	0.01	0.02	0.03	0.05	0.1	0.15	0.2	0.25	0.3	0.35	0.39	0.44
Deviation (%)	-5.9	-2.4	-1.5	2.7	3.9	-6.1	-6	-5.6	-6.1	-6.4	-6.4	-7.3

5 Conclusions

The flow process inside a lateral inlet pressure regulator has been investigated by commercial ANSYS FLUENT code. A mathematical model that features the inlet pressure and displacement to the outlet pressure is presented by the CFD approach. This model reveals the movement of the regulation assembly inside the regulator and provides the value of displacement that the experiment cannot directly provide.

On the basis of the simulated pressure induced force–displacement and the outlet pressure–displacement characteristics of the pressure regulator, a force–displacement characteristic (the F–L_v curve) that satisfies the designed preset pressure and flow rate requirements is obtained. This characteristic can be applied to the spring parameter design.

The details of the flow through the pressure regulator at various displacements provide an improved understanding of the force–displacement characteristic inside the pressure regulator. These findings are helpful in the design process.

Numerical results show that the regulation assembly inlet height is a key factor in pressure regulator design because the regulation assembly inlet height determines the pressure loss inside the regulator. Thus, the design should provide a balance between the performance requirement and production size.

References

1. Bernuth von, R.D., Baird, D.: Characterizing Pressure Regulator Performance. Transaction of ASAE 33, 145–150 (1990)
2. Tian, J., Gong, S., Li, G., et al.: Impacts of Pressure Regulator Parameters on Preset Pressure in Micro-irrigation System. Transactions of the CSAE 21(12), 48–51 (2005)
3. Mokhtanadeh-Dehghan, M.R., Ladommatos, N., Brennan, T.J.: Finite Element Analysis of Flow in a Hydraulic Pressure Valve. Applied Mathematical Modelling 21(7), 437–445 (1997)
4. Dempster, W., Lee, C.K., Deans, J.: Prediction of the Flow and Force Characteristics of Safety Relief Valves. In: Proceedings of PVP2006-ICPVT-11 2006 ASME Pressure Vessels and Piping Division Conference (July 2006)
5. Dempster, W., Lmayyah, W.E.: A Computational Fluid Dynamics Evaluation of a Pneumatic Safety Relief Valve. In: The 13th International Conference on Applied Mechanics and Mechanical Engineering (AMME (May 2008)
6. Han, X., Zheng, M., Yu, Y.: Hydrodynamic Characterization and Optimization of Contra-push Check Valve by Numerical Simulation. Annals of Nuclear Energy 38(6), 1427–1437 (2011)
7. Chattopadhyay, H., Kundu, A., Saha Binod, K., et al.: Analysis of Flow Structure Inside a Spool Type Pressure Regulating Valve. Energy Conversion and Management 53(1), 196–204 (2012)
8. Song, X., Park, Y., Park, J.: Blowdown Prediction of a Conventional Pressure Relief Valve with a Simplified Dynamic Model. Mathematical and Computer Modelling 57(1-2), 279–288 (2013)
9. Shahani, A.R., Esmaili, H., Aryaei, A., et al.: Dynamic Simulation of a High Pressure Regulator. Journal of Computational and Applied Research in Mechanical Engineering 1(1), 17–28 (2011)
10. Beune, A., Kuerten, J.G.M., Heumen van, M.P.C.: CFD Analysis with Fluid-Structure Interaction of Opening High-Pressure Safety Valves. Computers & Fluids 64(15), 108–116 (2012)
11. Song, X., Cui, L., Cao, M., et al.: A CFD analysis of the dynamics of a direct-operated safety relief valve mounted on a pressure vessel. Energy Conversion and Management 81, 407–419 (2014)

12. Song, X., Wang, L., Park, Y.: Transient Analysis of a Spring-Loaded Pressure Safety Valve Using Computational Fluid Dynamics (CFD). Transactions of the ASME 132, 054501/1–054501/5 (2010)
13. Jeon, S.Y., Yoon, J.Y., Shin, M.S.: Flow Characteristics and Performance Evaluation of Butterfly Valves Using Numerical Analysis. In: IOP Conference Series Earth and Environmental Science 12(012099), vol. (1), pp. 1–7 (2099)